Characterization of the 3M Scotch-Weld™ 7260 B/A epoxy adhesive by cohesive damage models and application to a full-scale bonded sub-structure

S. Cardamone, A. Bernasconi, M. Giglio

Politecnico di Milano, Dipartimento di Meccanica, Milan, Italy

Via G. La Masa 1, 20156 Milan, Italy. Email: andrea.bernasconi@polimi.it.

Abstract

One of the most challenging aspects of adhesive bonding is the prediction of failure of the joints. Cohesive damage modelling is one of the most advanced technique to predict failure of complex adhesively bonded parts by the finite element method. However, the parameters of the cohesive models are not usually provided by adhesives' manufacturers.

In this work, the 3M Scotch-Weld™ 7260 B/A two-component epoxy resin was characterized by experimental tests in loading modes I and II. Cohesive model parameters were derived through numerical optimizations.

Finally, the obtained cohesive models were applied to a full-scale bonded sub-structure and results compared with the experimental test. The analysis of the bonded sub-structure showed a good agreement with experiments in terms of stiffness and lead to underestimate by 11% the maximum load reached before failure.

Keywords

epoxy/epoxides; Cohesive damage models; epoxy; DCB test; ENF test; numerical optimization; FE simulation.

1

1. Introduction

Adhesive bonding is being increasingly used in various engineering fields and is particularly compliant with lightweight design principles. Adhesive bonding offers various advantages compared to mechanical connections. For example, adherends are not weakened by holes, load transmission is surface-related instead of spot-related, stresses are more evenly distributed, dissimilar materials and very thin parts can be connected. In general, adhesively bonded assemblies tend to be lighter and to save material costs [1, 2]. However, the lack of data provided by adhesive manufacturers and the difficulty to predict strength and failure of adhesives represent the most common challenges faced by engineers. Stress singularities in adhesive joints make stress-based approaches difficult to apply. Moreover, energy-based approaches allow to predict well crack propagation in the adhesive layer, but they assume the existence of a defect which must be artificially introduced in finite element models as a pre-crack [3].

In the recent years, to overcome these drawbacks and to exploit the advantages of the aforementioned approaches, cohesive damage models have been developed. They combine stress-based analysis, to model damage initiation, and fracture mechanics, to deal with damage propagation, without any initial crack length.

Elices et al. [4] presented advantages and limitations of this approach. Cohesive damage models are generally based on interface finite elements [5–13], called *cohesive element*s, which open when damage occurs, and lose their stiffness at failure, so that the adjacent continuum elements are disconnected [14]. This behaviour is managed by softening relationships between stresses and displacements, called Traction-Separation Laws (TSLs). This approach can be used for modelling fracture in homogeneous materials, like metals, but it is particularly suitable for simulating the delamination in composites or the damage and failure of adhesively bonded joints.

2

Currently, TSLs are implemented in various commercial software packages [15], but cohesive properties of adhesives are still not provided by manufacturers for various reasons: lack of standards that cover the derivation of all parameters, difficulties of experimental tests, large number of adhesives available from each manufacturer to be characterized and current low demand of these mechanical properties by users. Therefore, very often, the designer must experimentally determine the cohesive parameters needed for FE simulation with cohesive elements.

In the present work, the 3M Scotch-Weld™ 7260 B/A two-component epoxy resin (3M, Saint Paul MN, USA) was characterized at room temperature to identify its cohesive damage model parameters. Double Cantilever Beam (DCB) and End Notched Flexure (ENF) tests were performed to obtain the critical energy release rate values in loading modes I and II. The other cohesive parameters were derived through numerical optimization, run with the commercial software Isight™ (Dassault Sistèmes, Vélizy-Villacoublay, France), which iteratively modified the Abaqus™ (Dassault Sistèmes, Vélizy-Villacoublay, France) finite element models of the DCB and ENF tests, until the best match between numerical and experimental load-displacement curves was obtained. Finally, an experimental test of a full-scale bonded sub-structure, part of a real industrial application, bonded with the same adhesive, was performed. Results were compared with a numerical model of the bonded sub-structure, using the cohesive model parameters identified by DCB and ENF tests.

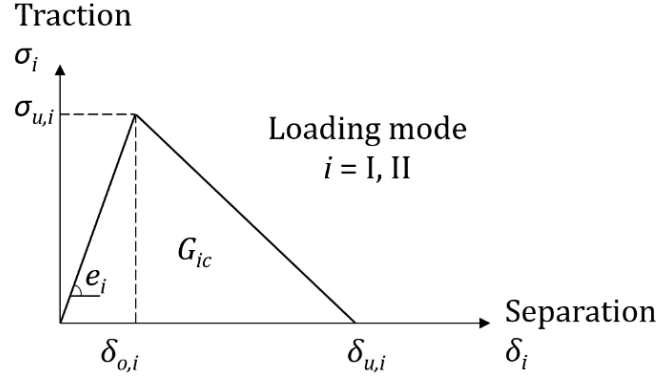## 2. Cohesive damage models

2.1. Traction-Separation Laws

Figure 1: Triangular Traction-Separation Law for a generic loading mode *i*.

Figure 1 shows a triangular TSL valid for a generic loading mode. This law relates stresses and displacements, either in tension or in shear, connecting paired nodes of the cohesive elements. Triangular TSLs are suitable for brittle adhesives, whereas trapezoidal shapes are more suitable for ductile adhesives [16–18]. The first part of the curve simulates the elastic behaviour up to the cohesive strength or ultimate stress ($\sigma_{u,I}$ in tension and $\sigma_{u,II}$ in shear). The second part represents the subsequent softening, allowing to model the degradation of material from the onset displacement ($\delta_{o,I}$ and $\delta_{o,II}$) up to the ultimate displacement ($\delta_{u,I}$ and $\delta_{u,II}$). The area under the curve is equal to the critical strain energy release rate (G_{Ic} and G_{IIc}), i.e. the amount of energy that a cohesive element can absorb before failure.

Undamaged strength evolution is defined in the commercial FE software used in this work (Abaqus™) by a constitutive matrix relating the current stresses **σ** and strains **ε** in tension and shear across cohesive elements [15, 17]:

$$\boldsymbol{\sigma} = \begin{Bmatrix} \sigma_I \\ \sigma_{II} \end{Bmatrix} = \begin{bmatrix} K_{nn} & K_{ns} \\ K_{sn} & K_{ss} \end{bmatrix} \begin{Bmatrix} \varepsilon_I \\ \varepsilon_{II} \end{Bmatrix} = \boldsymbol{K\varepsilon} \tag{1}$$

4

Since there is no coupling between normal and shear components, the non-diagonal parameters of matrix **K** can always be considered null. Furthermore, following Abaqus™ definitions, strains $\boldsymbol{\varepsilon}$ correspond to cohesive elements separations $\boldsymbol{\delta}$ divided by a constitutive thickness t_0 at each integration point, whose default value is 1. Considering these assumptions, Eq. (1) then becomes:

$$\boldsymbol{\sigma} = \left\{ \begin{matrix} \sigma_I \\ \sigma_{II} \end{matrix} \right\} = \begin{bmatrix} K_{nn}/t_0 & \\ & K_{ss}/t_0 \end{bmatrix} \left\{ \begin{matrix} \delta_I \\ \delta_{II} \end{matrix} \right\} = \begin{bmatrix} e_I & \\ & e_{II} \end{bmatrix} \left\{ \begin{matrix} \delta_I \\ \delta_{II} \end{matrix} \right\} = \boldsymbol{E}\boldsymbol{\delta} \qquad (2)$$

It is important to highlight that the constitutive thickness t_0 is different from the geometrical thickness t_A of the cohesive elements. The matrix **E** contains the stiffness parameters e_i, defined as the ratio between the elastic modulus of the material in tension or shear (E or G, respectively) and t_A:

$$e_I = \frac{E}{t_A} \qquad\qquad e_{II} = \frac{G}{t_A} \qquad\qquad (3)$$

The meaning of these stiffness parameters, which must be introduced in Abaqus™, depends on how the adhesive layer is modelled. In fact, two main strategies are available:

- *Local cohesive approach*: cohesive elements are used for modelling zero thickness fractures. In this case, $t_A = 0$, since zero thickness cohesive elements or cohesive behaviour contacts are used, while deformations of the physical adhesive layer are assigned to adjacent continuum FE elements. Therefore, e_i tend to infinite and lose their physical meaning: their values must be chosen as large as possible (compatibly with numerical analyses convergence), because cohesive elements must not interfere with the deformation of the adjacent parts. An example of application of this approach can be found in the work of Campilho et al. [19]. Some studies [20–22] assumed values of e_i equal to 10^6 or 10^7 MPa/mm, to help convergence and avoid numerical problems.

5

- *Continuum cohesive approach*: cohesive elements are used for modelling the whole adhesive layer. In this case, the cohesive element thickness t_A is equal to the physical thickness of the adhesive layer. Therefore, using $e_I = E$ and $e_{II} = G$ provides a good approximation of the mechanical behaviour of the adhesive [17]. An example of application of this approach can be found in the work of de Moura et al. [16].

Damage initiation under mixed-mode conditions can be specified by different criteria [17]. For instance, in the case of the quadratic nominal stress criterion, damage occurs when the condition set by Eq. (4) is reached:

$$\left(\frac{\langle \sigma_I \rangle}{\sigma_{u,I}}\right)^2 + \left(\frac{\sigma_{II}}{\sigma_{u,II}}\right)^2 = 1 \qquad (4)$$

If the damage initiation condition is fulfilled, the material stiffness initiates a softening process. Numerically, this is implemented by the relation:

$$\boldsymbol{\sigma} = (\mathbf{I} - \mathbf{D})\, \mathbf{E}\, \boldsymbol{\delta} \qquad (5)$$

where $\mathbf{I}$ is the identity matrix, whereas $\mathbf{D}$ is a diagonal damage matrix, containing the damage parameters that depend on value of the current relative displacements in mode I or II, δ_i, with respect to $\delta_{o,i}$, the onset relative displacements. Finally, the complete separation (identified by the point at $\delta_{u,i}$ in Figure 1) can be predicted by a fracture criterion, like the power law:

$$\left(\frac{G_I}{G_{Ic}}\right)^A + \left(\frac{G_{II}}{G_{IIc}}\right)^B = 1 \qquad (6)$$

where G_{Ic} and G_{IIc} are the critical fracture energy values in mode I and mode II, respectively. The linear energetic criterion, in which $A = B = 1$, and the quadratic energetic criterion, in which $A = B = 2$, are the most frequently used ones [3].

2.2. Evaluation of the cohesive parameters

A triangular TSL implemented with a continuum cohesive approach can be completely defined by three parameters for each loading mode, like G_{ic}, e_i and $\sigma_{u,i}$, or another combinations of three parameters. For mode I and mode II, the total number of cohesive parameters to be identified is six.

G_{Ic} and G_{IIc} certainly represent the most important cohesive parameters and those with the most meaningful physical properties. The mode I critical energy G_{Ic} can be calculated performing the standardized DCB test [23, 24], whereas G_{IIc} can be calculated by means of non-standardized mode II tests, for example by the ENF test, whose best practices can be found in [25]. Other strategies can be adopted for obtaining the critical energies, for example the J-integral method, derived from the theory independently developed by Rice [26] and Cherepanov [27]. This method was developed for adhesive joints by Olsson and Stigh [28]. An example of application was made by Andersson and Stigh [29]. The experimental setup required by the J-integral method differs from standard setups, as additional data like the rotations of the adherends need to be acquired during loading [17].

Regarding e_I and e_{II}, the identification of these parameters by tests on bulk adhesive specimen is questionable as bulk properties may differ from those of thin adhesive layers. Nevertheless, the elastic moduli E and G, respectively, represent a good approximation of these parameters in the continuum approach. Indications for manufacturing bulk specimens free of defects and, consequently, experimentally obtaining e_I and e_{II}, can be found in the literature [25,30]. Anyway, even when a local cohesive approach is used, these parameters are needed to correctly simulate the adjacent adhesive layer modelled by continuum elements.

Conversely, $\sigma_{u,I}$ and $\sigma_{u,II}$ do not correspond to properties of the adhesive as a bulk material [3]. Deviations have been reported between the cohesive properties of a bulk

7

adhesive and those of a thin adhesive layer. This is caused by the strain constraining effect of the adherends in bonded assemblies and by the typical mixed-mode crack propagation in adhesive bonds [29, 31–33]. In fact, in bulk materials, cracks tend to grow perpendicularly to the direction of maximum principal stress. Conversely, in thin adhesive layers, cracks are forced to follow the bondline, since failure is often cohesive within the adhesive, as the adhesive is typically weaker and more compliant than the components to be joined [19, 34].

Different methods have been reported in the literature for the evaluation of the cohesive parameters $\sigma_{u,I}$ and $\sigma_{u,II}$. They can be divided into inverse and direct methods.

Inverse methods are the most common ones and consist of iterative curve fitting between experimental tests and the corresponding FE simulations. Different experimental data were used for fitting: Flinn *et al.* [35] used the critical energy release rate G_c vs crack length a curve (R-curve), Mello and Liechti [36] used the crack opening profile, Li *et al.* [37] used the load P vs. displacement δ curve. Indeed, fitting the load-displacement curve is the most common procedure in the recent literature. The typical method used for fitting curves is a trial and error process, used, for example, by Campilho et al. [38]. Depending on the experience of the user, up to 20 or more simulations are necessary to achieve a reasonably good approximation of the experiment [8].

A more formal process consists of numerical optimisation methods by error minimisation. In this case, gradient methods and evolutionary algorithms can be used. Since the design space is continuous and smooth in a confined range, the chance of getting the global minimum from reasonable starting values makes gradient methods preferable for the identification of the cohesive parameters [8]. The criterion for identification is the minimisation of an object function that measures the difference between the experimental and the numerical values of the same entity (P, $G_{I, II}$ or a) as a function of displacement

or of another variable. A drawback for automated optimizations arises if the simulation does not converge. In this case, the resulting differences cannot be calculated, and the error calculation is inaccurate. Therefore, it is highly recommended to check if the simulation converges [8]. More complex algorithms can be used for fitting experimental and numerical curves, such as the neural networks. Details of this procedure applied to the evaluation of cohesive parameters can be found in [8].

Direct methods are based on the estimation of the cohesive parameters $\sigma_{u,I}$ and $\sigma_{u,II}$ by the direct differentiation of the G_I–δ_I and G_{II}–δ_{II} curves. Examples were given by Högberg and Stigh [31] and Carlberger and Stigh [39], in which the J-integral was derived from the test data by a formulation that required knowledge of the values of the adherends rotation at the loading point. As previously mentioned for the evaluation of G_{Ic} and G_{IIc} from the J-integral, this method requires more effort in experimental measurements, but it was demonstrated to be adequate.

3. Adhesive characterisation by cohesive damage models

3.1. Introduction on experimental testing

The adhesive analysed in this work is the 3M Scotch-Weld™ 7260 B/A two-component epoxy resin, which is available in four different versions [40, 41]. This work focused on the *NS* version, *NS* standing for Non-Sag. This contains a base component with higher viscosity (700-900 Pa·s) that prevents gravity-induced downward flow, given its thixotropic behaviour. All tests described in this work were conducted at room temperature.

The same adherends geometry and material were adopted for DCB and ENF tests. A high-strength steel DIN 40 CrMoMn7 was used, to avoid plastic deformation of the

adherends that might affect the evaluation of critical energies, particularly in ENF tests. Therefore, the yielding of the specimens must always be avoided [3]. Table 1 shows the mechanical properties of the used steel.

Table 1: Mechanical properties of DIN 40 CrMoMn7.

Tensile failure strength (MPa)	1000
Yield stress (MPa)	861
Elongation (%)	14–17
Young's modulus, E (GPa)	205
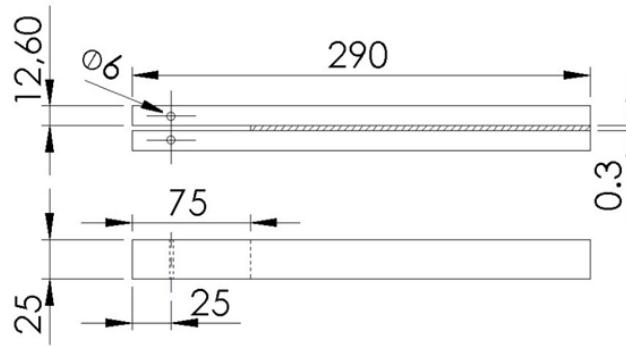
Figure 2: Specimen size (not to scale) of DCB and ENF tests.

Figure 2 shows the size of the specimen used for the evaluation of the fracture energies, consisting in two adherends connected by an adhesive layer. The height of the adherends and the position of the transversal holes were the ones recommended for DCB specimens by the standard ASTM D3433 [23]. ENF specimen sizes are not standardized, but, using the same geometries as for DCB tests and the high strength steel, no plastic deformation was experienced.

Adherends surface treatment consisted of sandblasting and cleaning. The degreasing/cleaning process was made with acetone before and after the mechanical surface preparation, to ensure the complete removal of particles, processing oils, grease or dirt.

10

An initial debonding of 75 mm from the specimen's edge was ensured by a polytetrafluoroethylene (PTFE) 0.1 mm thick tape that avoided any adhesive bond with the epoxy and ensured a reduced friction between parts during mode II tests. A static mixer ensured the required 2:1 mixing of the two adhesive components. The minimum bondline thickness was controlled by mixing the adhesive with glass microspheres, with a diameter between 250-300 μm (2% by weight of the adhesive). The adhesive was finally spread on the specimens with a metallic spatula. The alignment was ensured by means of a proper jig and the required pressure, as specified by the manufacturer [40, 41], was applied for the first 24 h. Curing was completed in oven for 3 hours at a temperature between 60-65°C, as specified by the manufacturer [40, 41]. After curing, solid spew adhesive was mechanically removed. Finally, a white spray paint was applied to the adhesive bondline to enhance the visibility of the crack tip, given the dark colour of the adhesive.

For all DCB and ENF specimens, a pre-cracking stage was carried out to ensure that the crack tip was sharper than the blunt tip created by the PTFE insert. This procedure was performed by a monotonic loading under pure mode I, with the same DCB setup described below, except for the test speed of 0.1 mm/min. This slower speed, at the lower limit of the speed values suggested by ISO 25217 standard [24], was chosen to ensure that, as soon as a drop in the measured load was detected, the test could be stopped. It must be pointed out that the sharpness of the crack tip can be affected by the test speed and a higher pre-cracking speed, e.g. equal to the test speed of 0.5 mm/min, might have reduced further the size of the plastic process zone.

This procedure provided an additional a_{pc} (crack length due to pre-cracking) of about 10 mm, to be added to the 50 mm initial length created by the PTFE tape, as schematized in Figure 3. Since a_{pc} was different from specimen to specimen, the total initial crack

length a_0 was measured before each test. An optical microscope was used to detect the crack tip and measure the initial crack length. Table 2 summarizes the test plan of all experiments in mode I and mode II.
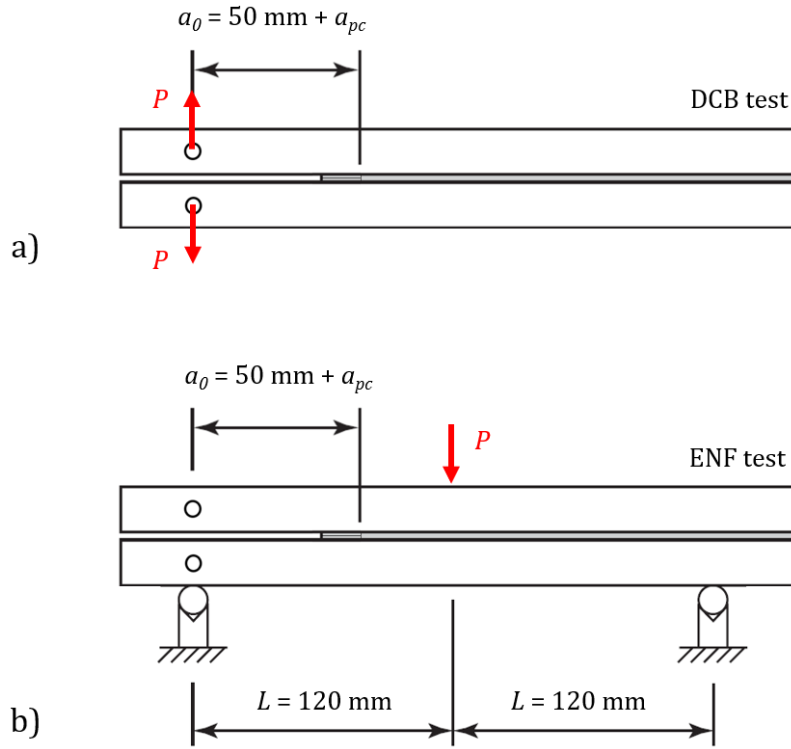

Figure 3: a) DCB test configuration; b) ENF test configuration.

Table 2: Summary of test plan.

Test type	Number of tests
DCB (mode I)	5
ENF (mode II)	4

3.2. Mode I experimental testing (evaluation of G_{Ic})

Setup and data reduction methods

DCB tests (Figure 3a) were performed using an MTS electro-mechanical testing machine of 150 kN capacity. The test speed was 0.5 mm/min, as suggested by the standard ISO 25217 [24]. Load P and machine's crosshead displacement δ_{cm} were recorded for every test.

Three different data reduction methods were used and compared to obtain G_{Ic}. The first two methods are those suggested by the ISO 25217 standard [24]: the Corrected Beam Theory (CBT) and the Experimental Compliance Method (ECM). According to CBT, derived from the Standard Beam Theory and based on the Euler-Bernoulli beam theory, the value of G_{Ic} can be obtained from:

$$G_{Ic} = \frac{3P\delta}{2b(a + |\Delta|)} \tag{7}$$

where b is the specimen width and Δ is a correction for crack tip rotation and deflection. Δ can be determined from a linear regression analysis of $(C)^{1/3}$ versus a data, C being the compliance (δ/P). According to the ECM, still based on a mathematical correction of the compliance, the value of G_{Ic} can be obtained from:

$$G_{Ic} = \frac{nP\delta}{2ba} \tag{8}$$

where n is the slope of $(log_{10}C)$ as a function of $(log_{10}a)$ data.

Additionally, the theory proposed by Krenk in 1992 [42] was used for the evaluation of G_{Ic}. In this case, the adhesive layer is modelled as a continuous distribution of independent springs, whereas adherends are schematized as simple beams. In this model, the propagation of a crack is simply equivalent to a shorter length of the adhesive. Following Krenk's model and considering the shear contribution to opening modelled by Timoshenko's beam theory, the opening displacement δ can be expressed as:

$$\delta = \frac{4P\lambda_\sigma}{k}\left[1 + 2\lambda_\sigma a + 2(\lambda_\sigma a)^2 + \frac{2}{3}(\lambda_\sigma a)^3 + \frac{12Pa}{5Ghb}\right] \tag{9}$$

The parameter λ_σ is associated to the bending stiffness of the beam on an elastic foundation is defined as:

$$\lambda_\sigma^4 = \frac{6}{h^3 t} \cdot \frac{E_a'}{E} \tag{10}$$

where t is the adhesive layer thickness, E is the Young's modulus of the adherends and E'_a is the bulk modulus of the adhesive, which can be calculated from E_a and v_a, the Young's modulus and the Poisson's coefficient of the adhesive respectively:

$$E_a' = \frac{E_a}{(1 - v_a^2)} \tag{11}$$

The parameter k represents the bending stiffness of an individual spring of the model:

$$k = \frac{2E_a' b}{t} \tag{12}$$

Regarding the strain energy release rate, starting from the Irwin-Kies's equations, it is possible to derive the value of G_{Ic}:

$$G_{Ic} = \frac{(Pa)^2}{bEJ}\left(1 + \frac{1}{\lambda_\sigma a}\right)^2 \tag{13}$$

where $J = bh^3/12$ is the moment of inertia of a single adherend of height h.

In the mode I experimental tests, G_{Ic} was calculated by Eq. (7), Eq. (8) and Eq. (13). Krenk's data reduction method requires the values of the Young's modulus E_a and the Poisson's coefficient v_a of the adhesive. Typical values of similar two-component epoxies were used, since the manufacturer does not provide these properties, therefore 2500 MPa and 0.35 were assumed for E_a and v_a, respectively. In any case, it was found that slightly different values did not influence the resulting G_{Ic}.

For all data reduction methods, the crack length a was analytically calculated by Krenk's model, using Eq. (9), which relates a to P and δ. Rewriting the equation in terms of the variable a, it becomes:

$$\left(\frac{8P\lambda_\sigma^4}{3k}\right)a^3 + \left(\frac{8P\lambda_\sigma^3}{k}\right)a^2 + \left(\frac{8P\lambda_\sigma^2}{k} + \frac{12P}{5hbG_{12}}\right)a + \left(\frac{4P\lambda_\sigma}{k} - \delta\right) = 0 \tag{14}$$

14

Eq. (14) is written as a third order equation having constant terms that depends on material and geometry of adherends and adhesive, in which a is the unknown variable:

$$K_1 a^3 + K_2 a^2 + K_3 a + K_4 = 0 \qquad (15)$$

K_1, K_2, K_3 and K_4 being non-null distinct coefficients, it is possible to calculate the closed-form solution:

$$a = \frac{\sqrt[3]{\sqrt{(C_1)^2 + 4(C_2)^3} + C_1}}{3K_1 \sqrt[3]{2}} - \frac{K_2}{3K_1} - \frac{\sqrt[3]{2}(C_2)(3K_1)^{-1}}{\sqrt[3]{\sqrt{(C_1)^2 + 4(C_2)^3} + C_1}} \qquad (16)$$

where:

$$C_1 = -27K_1^2 K_4 + 9K_1 K_2 K_3 - 2K_2^3 \qquad (17)$$
$$C_2 = 3K_1 K_3 - K_2^2$$

This analytical method of crack length calculation was validated by additional DCB tests performed on the *FC* version of the used epoxy [40,41] (*FC* standing for *Fast Cure*), having also a lower viscosity of the base component (100-300 Pa·s). The other mechanical properties of the *FC* version are close to those of the *NS* epoxy used for the tests of the present work. The use of the FC version for the validation of the crack length calculation is due to the temporary unavailability of the NS version during the initial set-up.

The validation was obtained by comparing the analytically calculated crack length with the actual crack length, experimentally measured by means of an optical camera during all the propagation phase. Figure 4 shows the superposition of the experimental and analytical *P-a* curves. The analytically calculated *a* and the experimentally measured *a* are drawn by a continuous line and a dashed line, respectively. Dots represent the point at which the crack length was measured through the optical camera video.

The analytically calculated values of *a* are very close to experimental ones. The small difference lead to a negligible overestimation of G_{Ic} and allowed for much less time-

15

consuming DCB tests. Therefore, for the following tests on the NS version, installation and use of the optical camera was avoided.
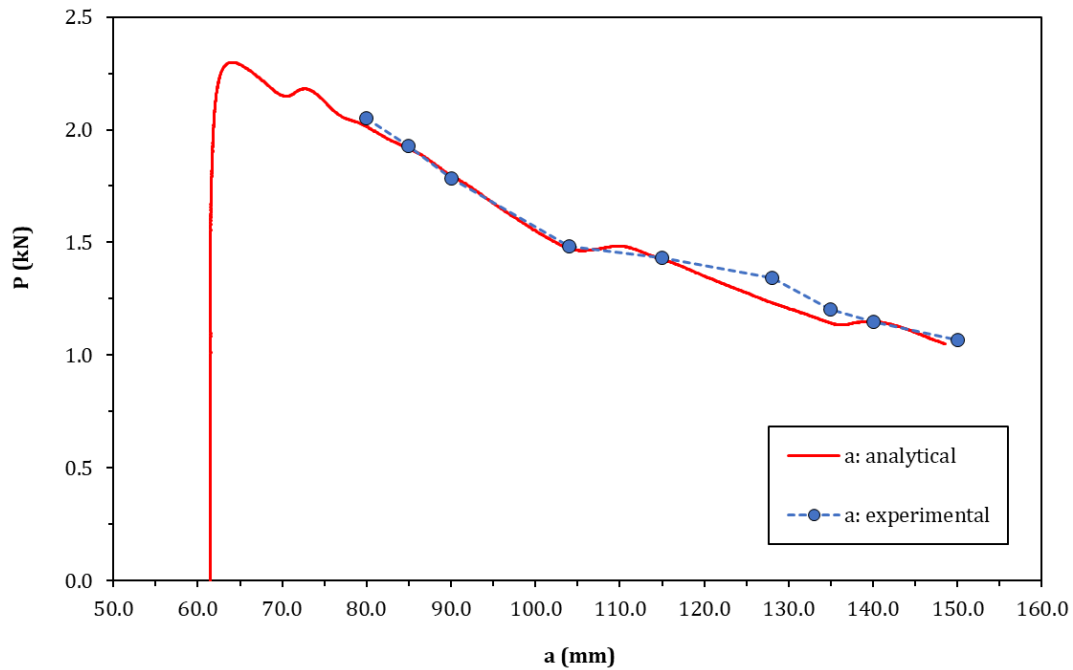

Figure 4: Load vs. crack length curves: comparison of analytical and experimental values for the FC epoxy.

Results and discussion

Figure 5 shows the results of one of the five DCB tests performed on the NS epoxy, in terms of load vs. displacement. The contribution of the initial clearance and of the compliance of the gripping system was already excluded from the experimental data. Moreover, the data range in which G_{Ic} was calculated is highlighted in Figure 5. This range, taken from the peak load to the release point, corresponds to the fracture propagation in the adhesive bondline. All the DCB tests showed a clear cohesive failure.
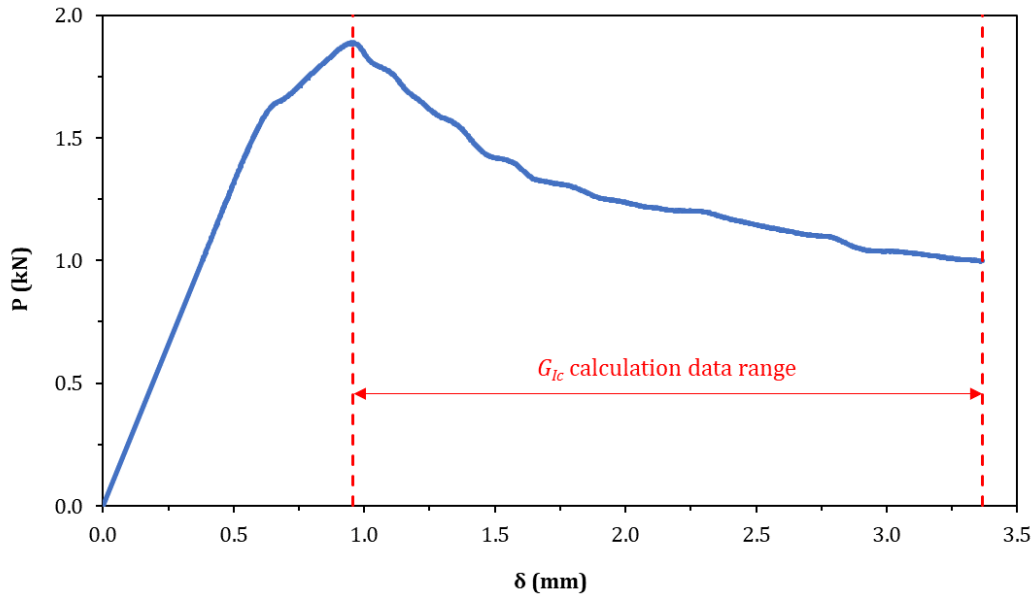
Figure 5: Experimental load vs. displacement of a DCB test on the 3M 7260 B/A NS epoxy.

Table 3 shows the resulting G_{Ic} values, obtained using the three previously described data reduction methods. The average value of the critical energy can be evaluated as 1.07 N/mm.

Table 3: G_{Ic} values (N/mm) of the 3M 7260 B/A NS epoxy.

Test number	G_I calculation method			Mean
	Krenk	CBT	ECM	
Test 1	1.18	1.18	1.17	1.18
Test 2	1.10	1.10	1.07	1.09
Test 3	1.01	1.01	0.99	1.01
Test 4	0.99	0.99	0.96	0.98
Test 5	1.09	1.09	1.06	1.08
Mean	1.07	1.07	1.05	1.07
2σ variance	0.15	0.15	0.16	0.16

The mode I R-curves corresponding to the same DCB test of Figure 5, are shown in Figure 6. The corresponding data range for the calculation of G_{Ic} is highlighted in Figure

17

6. It is worth noting that this range corresponds to an approximately stable value of G_I, in agreement with results reported in the literature [3].
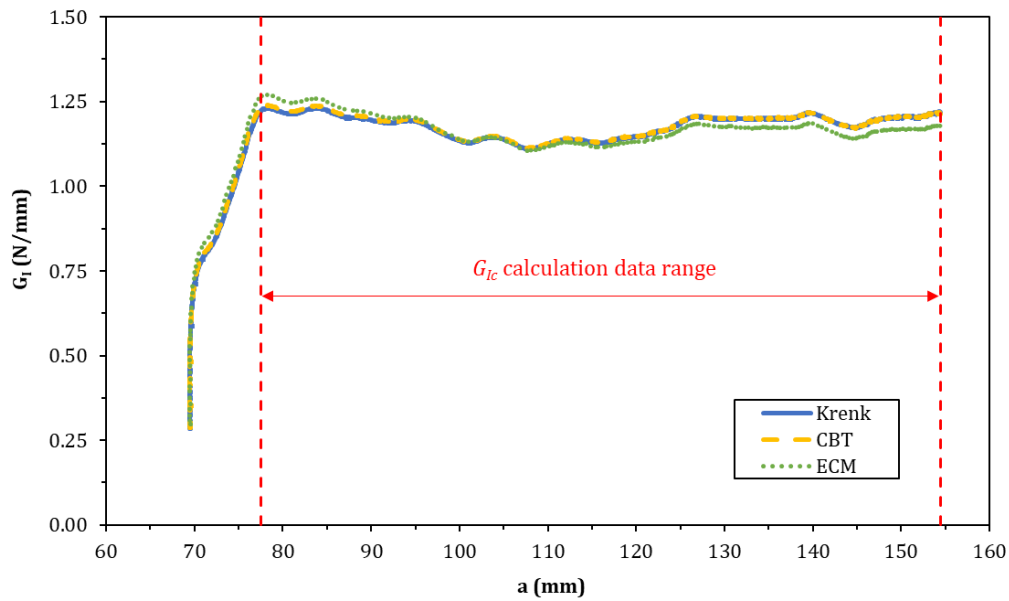

Figure 6: Strain energy release rate vs. crack length of a DCB test on the 3M 7260 B/A NS epoxy.

The three theoretical methods estimate the same initial crack a_0 of about 69 mm. It is worth to mention that the a_0 measured at the microscope, at the end of the pre-cracking stage, was 64 mm. The 5 mm difference can be attributed either to a crack tip excessively thin to be visible at the microscope or to an overestimation of a_0 by all analytical models.

3.3. Mode II experimental testing (evaluation of G_{IIc})

Setup and data reduction methods

ENF tests were performed using the same MTS electro-mechanical testing machine, of 150 kN capacity, used for the DCB tests. Since this test is not standardized, the best practices found in the literature were followed for obtaining reliable results [25]. The mode II setup consisted of a three-point bending configuration. Cylinders with a diameter of 6.4 mm were used for all experiments. The speed test was 0.5 mm/min and the span *2L* was 240 mm, as schematized in Figure 3b. A deflectometer placed in the middle point

of the lower surface of the specimen allowed to measure directly the vertical displacement δ of the specimen without calculating the system compliance. During the tests, the load P was recorded as well.

Regarding the calculation of G_{IIc}, the use of the Compliance Based Beam Method (CBBM) allowed to avoid the crack length measurement during the tests. Direct measurement of the crack length is difficult because the fracture propagates in pure mode II without showing any opening. Furthermore, the Fracture Process Zone (FPZ) effects, such as plasticity and micro-cracking, which are usually more pronounced in mode II tests, are included in the fracture energy measurement [3].

The CBBM is based on the beam theory and Castigliano's theorem. Following this theory, the equation of compliance can be derived:

$$C = \frac{3a^3 + 2L^3}{8E_f bh^3} + \frac{3L}{10Gbh} \tag{18}$$

where G is the shear modulus of the adherends. Since the flexural modulus of the specimen plays a fundamental role on the P–δ relationship, it can be calculated by Eq. (18) using the initial compliance C_0 and the initial crack length a_0:

$$E_f = \frac{3a_0{}^3 + 2L^3}{8bh^3 C_{0corr}} \tag{19}$$

where C_{0corr} is given by:

$$C_{0corr} = C_0 - \frac{3L}{10Gbh} \tag{20}$$

This procedure takes into account the variability of the material properties between different specimens and several other effects that are not included in beam theory: the stress concentrations near the crack tip, the contact between the specimen arms at the pre-crack region and the root displacement and rotation effects [16]. These phenomena affect the P–δ curve, even in the elastic regime. Using this methodology, their influence is accounted through the calculated flexural modulus E_f. It is worth to highlight that the

19

flexural modulus of the specimen is not an input property but a computed one. It is a function of the initial compliance C_0 and G, which is the only material property needed in this approach. However, de Moura *et al.* [43] showed that G has much less influence than the longitudinal modulus, which means that a typical value of G can be used. In this case, a value of 79.2 GPa was adopted for G and a value of 175 GPa for E_f was evaluated from the initial compliance.

Using E_f from Eq. (19), instead of E in Eq. (18), an *equivalent crack a_e*, accounting for the FPZ effects, is achieved as a function of the beam compliance ($C = \delta/P$) which varies during propagation:

$$a_e = a + \Delta a_{FPZ} = \left[\frac{C_{corr}}{C_{0corr}} a_0^3 + \frac{2}{3}\left(\frac{C_{corr}}{C_{0corr}} - 1 \right) L^3 \right]^{1/3} \tag{21}$$

where C_{corr} is given by Eq. (20) using C instead of C_0. G_{IIc} can be finally obtained using the Irwin-Kies's relation:

$$G_{IIc} = \frac{9P^2 a_e^2}{16 b^2 E_f h^3} \tag{22}$$

Results and discussion

Table 4 shows all resulting G_{IIc} values: the critical energy can be estimated as 6.63 N/mm. In Table 4, also the initial crack length a_0 is shown, as determined by the observation of the fracture surface of the specimens, once the adherends were separated at the end of tests. All the ENF tests showed a cohesive failure, confirmed by SEM observations of the failed surfaces.

Table 4: a_0 and G_{IIc} values of the 3M 7260 B/A NS epoxy.

Test number	a_0 (mm)	G_{IIc} (N/mm)			
		Mean	2σ variance	5th percentile	95th percentile
Test 1	62	6.51	0.77	5.88	7.08
Test 2	67	6.73	0.80	6.09	7.34
Test 3	63	6.66	0.74	6.03	7.21
Test 4	64	6.63	0.68	6.08	7.15
Mean		6.63	0.75	6.02	7.20
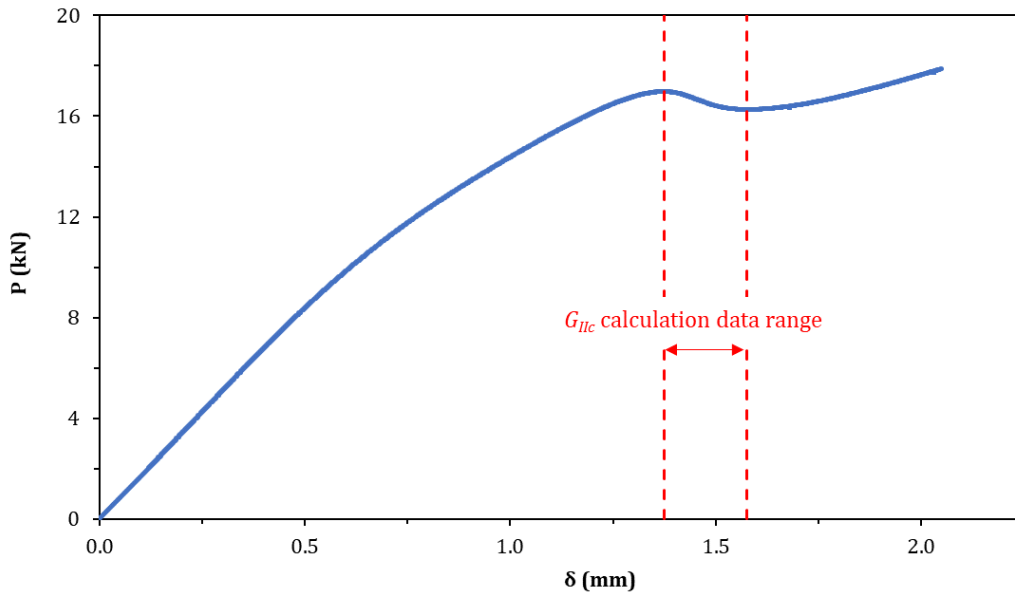
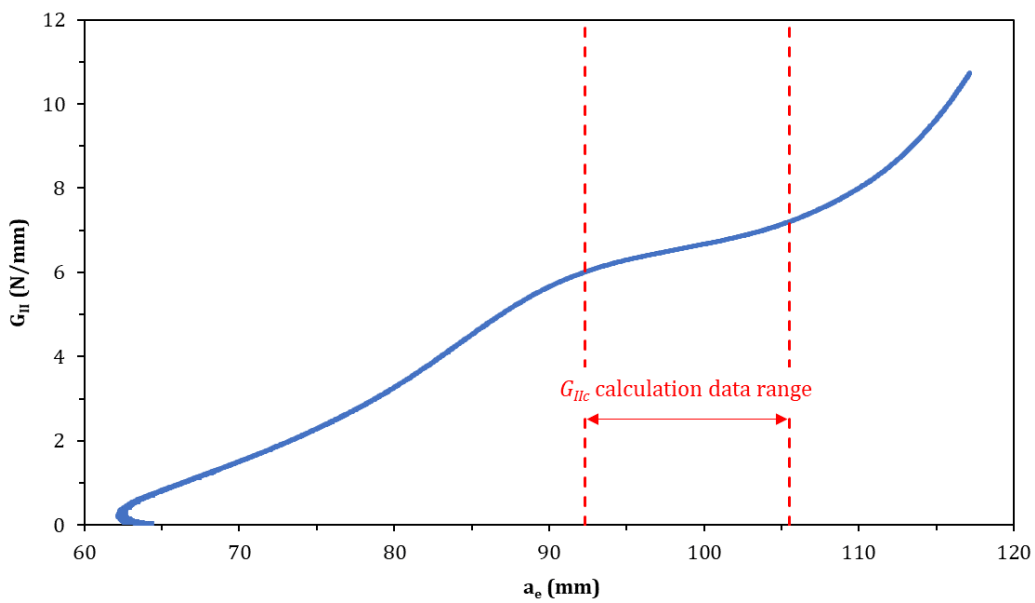**Figure 7: Experimental load vs. displacement of an ENF test on the 3M 7260 B/A NS epoxy.**

Figure 8: Strain energy release rate vs. equivalent crack length of an ENF test on the 3M 7260 B/A

NS epoxy.

Figure 7 shows the P-δ curve of one out of the four ENF tests, whereas the corresponding mode II R-curve is plotted in Figure 8. G_{IIc} can be estimated by the plateau of the curves in the last graph, representing the value of the energy released during a stable crack propagation [3]. In order to apply the same method to all ENF tests, the value of G_{IIc} was considered to be the average of the G_{II} values evaluated in the range from the

peak load to the valley in the P-δ curve, as highlighted in Figure 7. Accordingly, in Figure 8, the corresponding part of the R-curve is the most horizontal section. For the sake of completeness, 2σ variance, 5th and 95th percentile of G_{IIc} values of every single test are reported in Table 4.

The shape of P-δ and R-curves was approximately the same for all tests. As shown in Figure 8, all ENF specimens displayed first a decreasing value of the calculated crack length (occurred before about $\delta = 0.5$ mm in Figure 7), followed by a stable propagation with increasing values of G_{II}. Then the crack tip experienced an almost constant G_{II} close to the critical value. Afterward, the specimen showed a drop in the load P, as an unstable crack propagation occurred. After this drop, the load increased again, since the crack propagation decreased its speed and the specimen accumulated energy in a pronounced bending deformation, especially when the crack approached the loading cylinder. In the R-curve, this corresponds to an increasing slope of $G_{IIc} = f(a)$. At this point the test was stopped to avoid yielding of the adherends. However, no plastic residual deformation of the adherends was observed.

All R-curves were almost identical despite their different starting points, only due to different initial crack lengths, determined by the pre-cracking stage. It is worth to mention that the starting points of the R-curve perfectly matched the a_0 values measured on the fracture surface. After these initial points, the CBBM estimated, only for very low values of G_{II}, decreasing crack lengths. Obviously, this did not correspond to a real phenomenon: this misinterpretation by the data reduction method still does not have a clear explanation and it might be attributed to a limit of the CBBM model. However, the rest of the R-curve estimated by the CBBM is considered to be reliable, as the value of the final crack propagation length perfectly matched that observed on the fracture surface.

23

3.4. Numerical modelling of mode I-II tests (evaluation of e_i and $\sigma_{u,i}$)

In this section, the identification of the stiffness parameters e_I and e_{II}, as well as of the ultimate stresses $\sigma_{u,I}$ and $\sigma_{u,II}$ is described. The work consisted into simulating the experimental tests performed in pure mode I and II, by means of the Standard solver of the commercial FE software Abaqus™. The parameters were then obtained by a numerical optimisation method with error minimisation between experimental and numerical P-δ data. This process was carried out by means of the software Isight™.

DCB test model

The assembly of the DCB numerical model is shown in Figure 9a. The same geometry of the experimental tests was used. It is worth to highlight that a different initial crack length a_0 was considered depending on the simulated experimental test. Details of the mesh, close to the crack tip, are shown in Figure 9b. at different scales. An important feature of cohesive models is that there is no need to refine the mesh at the crack tip, since the approach is not based on stresses at the crack tip, provided that the mesh size is small enough to obtain a continuous Process Zone (PZ).
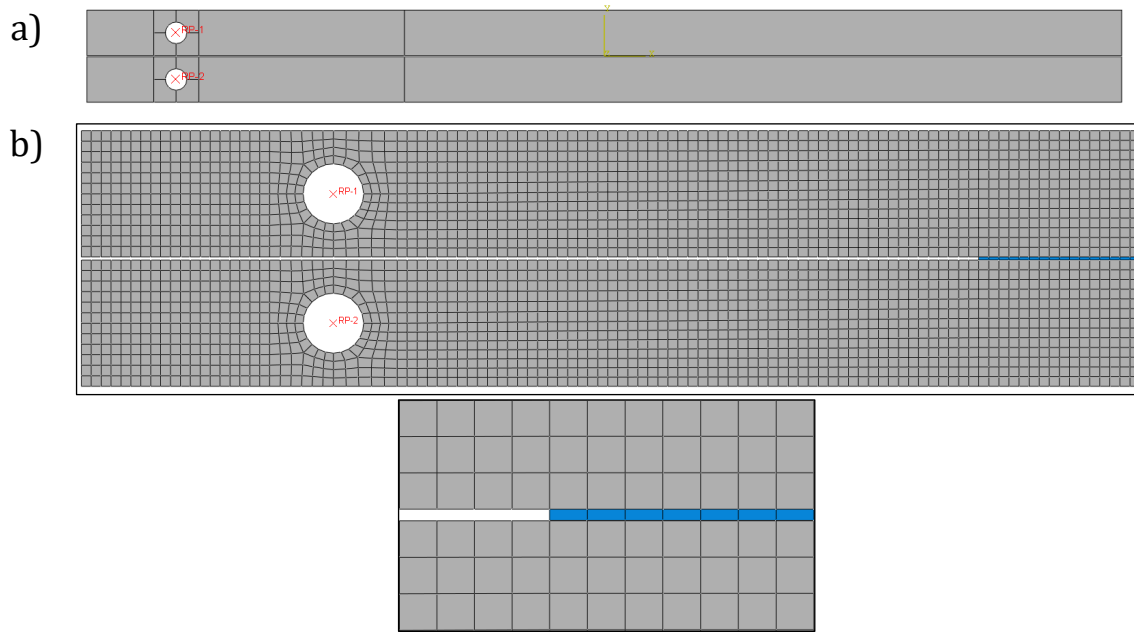
24

Figure 9: (a) Numerical model of the DCB test; (b) Details of the DCB numerical model.

The adherends were modelled using linear plane-stress quadrilateral elements of type CPS4R with reduced integration. Even though the hypothesis of plane-stress does not completely match the reality, especially in the middle of the specimen, the opposite plane-strain condition is even less realistic in this case. Nevertheless, the two conditions were compared and only a negligible difference was found in the results. Cohesive modelling is mesh-independent for reasonable mesh sizes, i.e. when a continuous PZ is achieved. Therefore, a maximum size of about 1 mm x 1 mm was chosen for the finite elements and the mesh-dependency was investigated around this value (from 0.5 to 2.5 mm) without showing any distinguishable influence on P-δ and R-curve results. For coarser mesh sizes (above 4 mm), P-δ was affected in the propagation region, showing oscillations with triangular waveform around the experimental value, due to a discontinuous PZ. For even larger element sizes, which approached the PZ size (about 15 mm), the simulations aborted because of numerical convergence problems. Material properties of the adherends correspond to the high-strength steel DIN 40 CrMoMn7 properties reported in Table 1.

25

An elastic-perfectly plastic behaviour was considered, with a yield stress limit of 861 MPa.

The adhesive was simulated using a single layer of COH2D4 cohesive elements (represented in blue in Figure 9b) with a behaviour defined by a TSL. A triangular shape of this softening relationship was chosen, since the behaviour of the epoxy was known to be mostly brittle. The mixed-mode conditions do not influence the behaviour of the specimen, since it is loaded in pure mode I. The average value of G_{Ic}, reported in Table 3, was implemented. A continuum cohesive approach was chosen for cohesive elements, since a finite thickness of 0.3 mm (the highest value of the actual adhesive thickness ensured by the glass microspheres mixed with the epoxy) was assigned to them.

The adhesive and the two adherends were modelled as three independent parts, connected by kinematic constraints that impose the same displacements to the nodes of the mating surfaces. In Abaqus™, this constraint is named *tie* and requires the definition of a *master* and a *slave* surface. Nodes of the slave surface are projected onto the master surface and displacements of the nodes of the slave surface are imposed equal to those of their projection points. If the position of the nodes of the slave surface coincides with that of the nodes of the master surface, this constraint is equivalent to merging the nodes of the two surfaces. However, the tie constraint was preferred to node merging because it allows for better managing the assembly and assigning the properties to the parts.

A vertical displacement was applied to the upper pin, defined by the reference point RP1, visible in Figure 9a and Figure 9b. Conversely, the lower pin, defined by reference point RP2, was fixed along all the translational degrees of freedom. These points were connected to the respective holes by a continuum distributed coupling, allowing for a rotation of the specimen around the centre of the hole. The resulting load *P* and

26

displacement δ were evaluated at the reference points. Finally, geometrical non-linearities were always considered in the numerical analyses.

ENF test model

The FE model of the ENF test was created following the same procedure as for the DCB numerical model, previously described. Figure 10 shows the whole model of the test, whereas Figure 11 highlights some details of the mesh and the different parts.
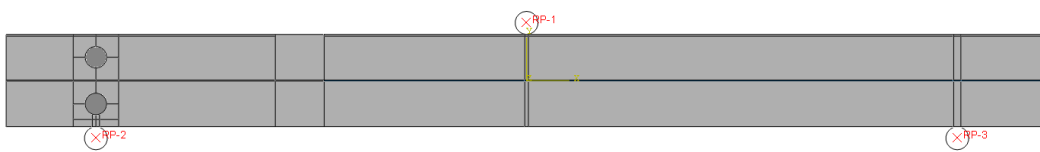

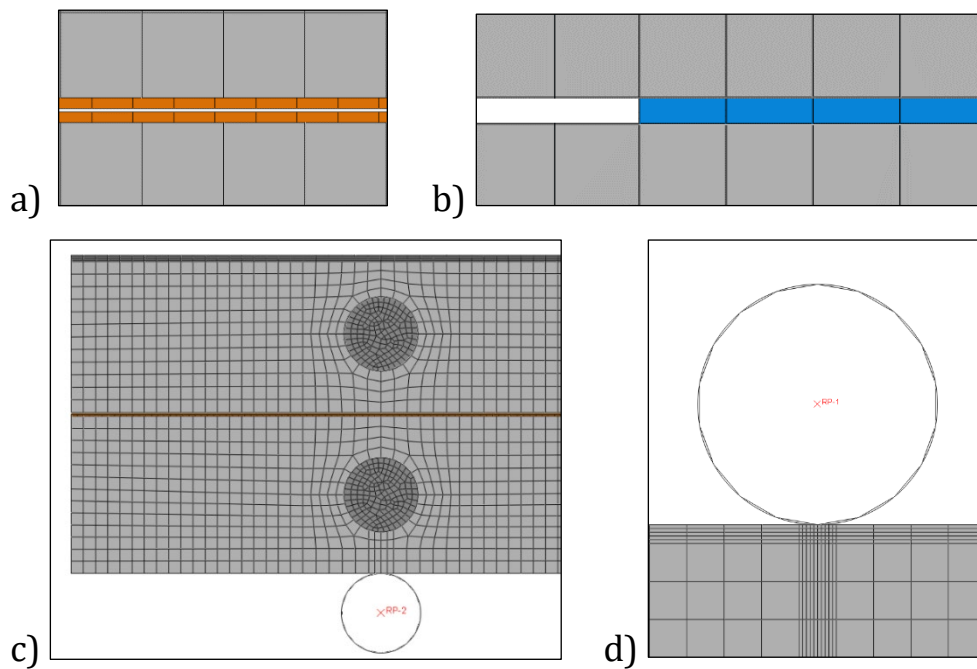**Figure 10: Numerical model of the ENF test.**

Figure 11: Details of the ENF numerical model.

The geometry of the adherends were the same as that of the DCB model. This time, the pins placed inside the holes, recognizable in Figure 11c, were modelled as solid parts to better simulate the elasticity of the assembly over the supporting rolls. In facts, the

27

rigid kinematic couplings used for the DCB specimen were appropriate for applying loads and enforcing boundary conditions to the displacements, but they would have made the model of the ENF specimen too stiff. The pins were then connected by coupling interactions to the adherends, as in the case of DCB specimen. The supporting and loading cylinders were simulated by rigid surfaces (R2D2 elements) and the contact with the adherends was modelled with a friction coefficient of 0.2 (typical of steel-to-steel contacts) in the tangential direction.

In order to correctly simulate the sliding of the two adherends, especially during the propagation of the adhesive fracture, the PTFE tape strips were modelled (orange layers in Figure 11a) and attached to the adherends by tie constraints. A contact with a friction coefficient of 0.01 (typical of PTFE-to-PTFE contact) was defined between the two PTFE layers, which came into contact as soon as the adherends bending became pronounced. Finally, loads and displacements of the upper cylinder were recorded. As resulted from DCB simulations, also ENF showed mesh size independency on P-δ and R-curve results around the chosen value of 1 mm. However, discontinuous PZ and inaccuracy in P-δ output occurred for element sizes larger than 2.5 mm, and even no fracture propagation was experienced for element sizes larger than 10 mm, as approaching the value of PZ size (about 37 mm).

Traction-Separation Laws optimization

Cohesive parameters that were not evaluated directly by experimental tests, i.e. stiffness parameters, e_I and e_{II}, and ultimate stresses, $\sigma_{u,I}$ and $\sigma_{u,II}$, were obtained by numerical optimization using Isight™.

A first Data Exchanger module writes the input file needed for the Abaqus™ simulation with the values of cohesive parameters updated iteratively by the optimization

process. For the first iteration, the initial values of e_i and $\sigma_{u,i}$ are arbitrarily chosen within a reasonable range. The numerical simulation is then run with Abaqus™. A second Data Exchanger-module collects the resulting loads and displacements from the simulation output and build the numerical P-δ curve that is compared with the experimental one. This last step is made by a Data Matching module, that calculates the sum of the squared difference between the experimental and numerical curves. Finally, an Optimization module updates the values of cohesive parameters for the following iteration, with the target of minimizing the previously calculated sum of the squared difference:

$$f = \sum_{i=1}^{n} \left(P_i^{exp} - P_i^{sim} \right)^2 \tag{23}$$

where n is the number of sampling points, P_i^{exp} and P_i^{sim} are the values of measured experimental and numerical load, obtained by tests and simulations, respectively. The chosen optimization algorithm was the Hooke-Jeeves direct search. It consists in a direct penalty method well-suited for long running simulations. A more complete description of numerical direct search methods can be found in the review paper by Torczon et al. [44]. The maximum number of iterative evaluations was set to 100 and it was never exceeded before the optimal values of cohesive parameters were found with a tolerance less than $\pm$ 0.05% for both e_i and $\sigma_{u,i}$. It is worth to mention that some mode II simulations ended finding more than one local minimum of the target function. Therefore, the user had to choose the best initial values of the cohesive parameters for the iterative process and the most appropriate range in which the experimental and numerical curves were compared.

Figure 12 schematizes an example of automatic data matching. The numerical curve of the first attempt does not perfectly matches the experiment. After less than 100 iterations, the optimized numerical curve matches the target and the optimized cohesive

29

parameters are obtained. Figure 13 shows the contour lines of the target function and the position of the optimum point in the design space of the cohesive parameters.
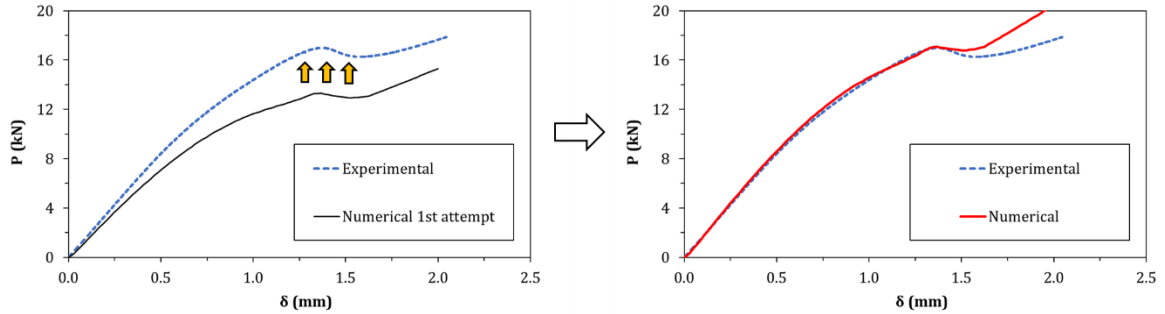

Figure 12: Example of automatic data matching of experimental and numerical curves.
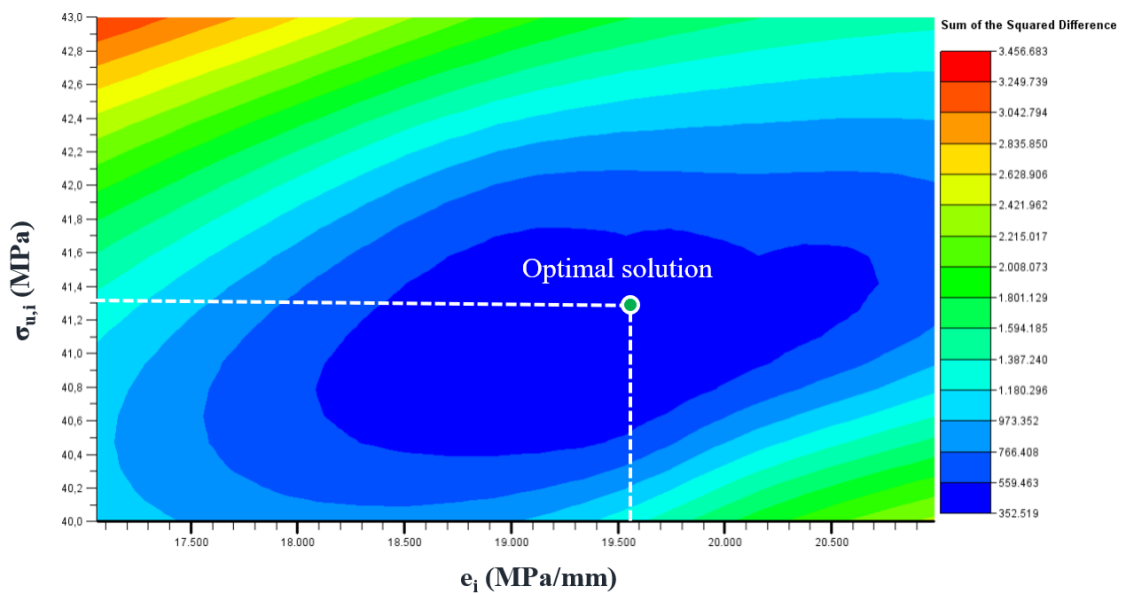

Figure 13: Example of resulting optimal solution located at the minimum of the target function.

The results of the comparison between experimental and numerical P-δ curves of DCB and ENF tests are shown hereafter. The optimization was conducted considering one curve only for the NS epoxy, selected as the most representative. Figure 14a and Figure 14b show the experimental-numerical comparison of the DCB and ENF tests, respectively.

30

It appears that the optimized numerical curve matched very well the experimental one in mode I. Not only were the initial stiffness and the maximum reached load correctly simulated, but also the crack propagation phase. In mode II, results are satisfactory as well, except for the final part of the curve, after the unstable crack propagation in the adhesive layer. Table 5 summarises the obtained cohesive parameters of the triangular TSL of the NS epoxy and the cohesive PZ size, i.e. the zone in which cohesive elements suffered damage, when stable propagation occurred.

Table 5: Optimized cohesive parameters of the 3M 7260 B/A NS epoxy.

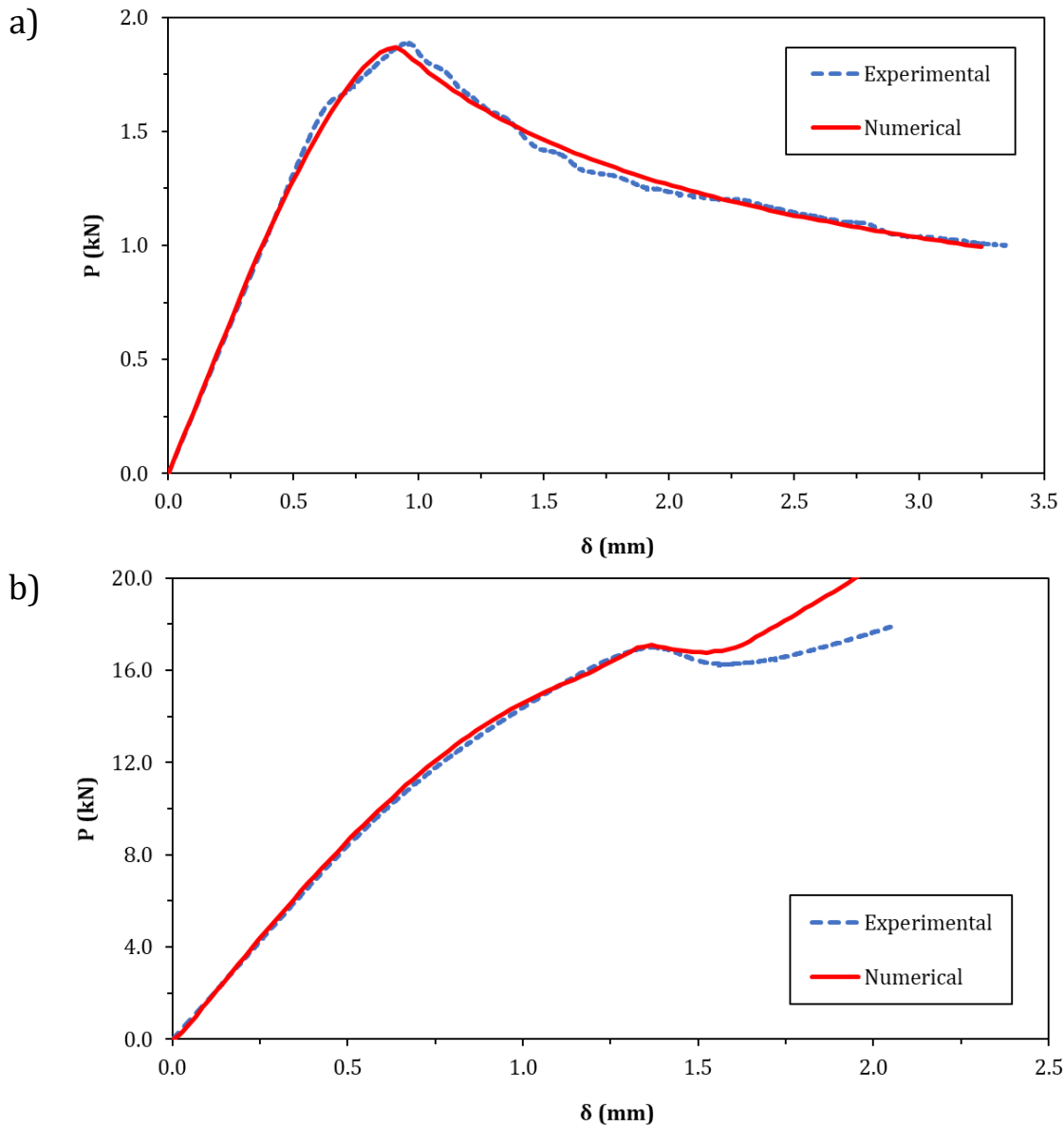| Loading mode	e_i (MPa/mm)	$\sigma_{u,i}$ (MPa)	Cohesive PZ size (mm)
Mode I	2114	26.13	15 ± 1
Mode II	19567	41.32	37 ± 1

Figure 14: Experimental-numerical comparison of the load vs. displacement curve of a DCB test (a) and an ENF test (b).

4. Application of the cohesive damage model to a full-scale bonded sub-structure

In order to prove the effectiveness of the cohesive damage model approach and, more specifically, to verify the previously obtained triangular TSL, defined by the cohesive parameters listed in Table 5, an experimental test on a specimen reproducing a full-scale

adhesively bonded sub-structure was conducted and simulated using the Standard solver of the software Abaqus™. This sub-structure was adopted for the construction of large panels, for a real application where high stiffness was a strong requirement that could be satisfied using adhesive bonding instead of mechanical joints. For this application, the adhesively bonded sub-structure was used to replace a riveted one, using the 3M 7260 B/A NS epoxy.

4.1. Experimental setup

Figure 15a shows the shape and the dimensions of the bonded sub-structure: the parts to be connected were two 1.5 mm thick panels made of DD11 steel [45]. The panels are bent in correspondence of one edge into a Z- or C-bend, so that the Z-bend of the first panel matches the corresponding C-bend of the other panel. A thin layer of 3M 7260 B/A NS epoxy ensured the connection between the two panels. The minimum bondline thickness was controlled by mixing the adhesive with glass microspheres, with a diameter in the 250-300 μm range. The adhesive bonding procedure was similar to that of the DCB and ENF specimens, except for the manual abrasion of the surfaces with the abrasive pad 3M CF-SR (instead of the sandblasting process, not feasible because of the size of the sub-structure) and for the use of clamps to maintain the alignment of the specimen during curing, carried out at approximately 25°C for 28 days.

Figure 15b shows the setup of the static experimental test performed on the sub-structure. A dedicated gripping system made of thick steel plates and bolts ensured the connection between the sub-structure and an MTS hydraulic testing machine of 100 kN capacity. The sub-structure was loaded perpendicularly to the plane of the adhesive layer, controlling the displacement of the machine's crosshead. In order to exclude the contribution of the gripping system and the testing machine crosshead from the obtained

33

experimental compliance, the stiffness of this test setup was measured. A simple 1.5 mm thick panel made of DD11 steel was connected to the gripping system and loaded up to the maximum load reached during the test on the full-scale sub-structure. Therefore, the actual displacement of the ends of the full-scale sub-structure could be obtained from the measured displacement of the testing machine's crosshead.
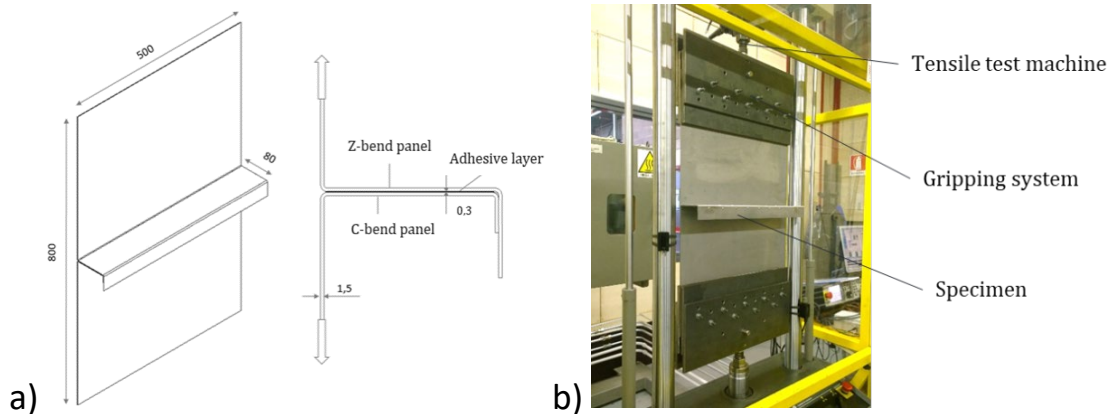

Figure 15: a) Adhesively bonded sub-structure design and size; b) Setup of the experimental test.

4.2. Numerical model

A mid-section of the adhesively bonded sub-structure was modelled with 2D elements, as shown in Figure 16. Since the width of the specimen was considerable (500 mm), this time plane-strain elements were used (CPE4R elements with reduced integration). The minimum size of the elements was 0.5 mm for the steel parts and 0.25 mm for the adhesive. Possible mesh-dependency was investigated around these values showing a negligible influence, also varying the ratio between the number of elements in the adhesive layer and those in the adherends. When using element of size larger than 4 mm, approximately the value of the PZ size, P-δ results became inaccurate. For even coarser mesh sizes (about 10 mm), no fracture propagation resulted from FE analyses.

34

The DD11 steel was modelled as elastic-plastic, using the flow curve (true stress-plastic strain) obtained from a tensile test, reported in Figure 17.
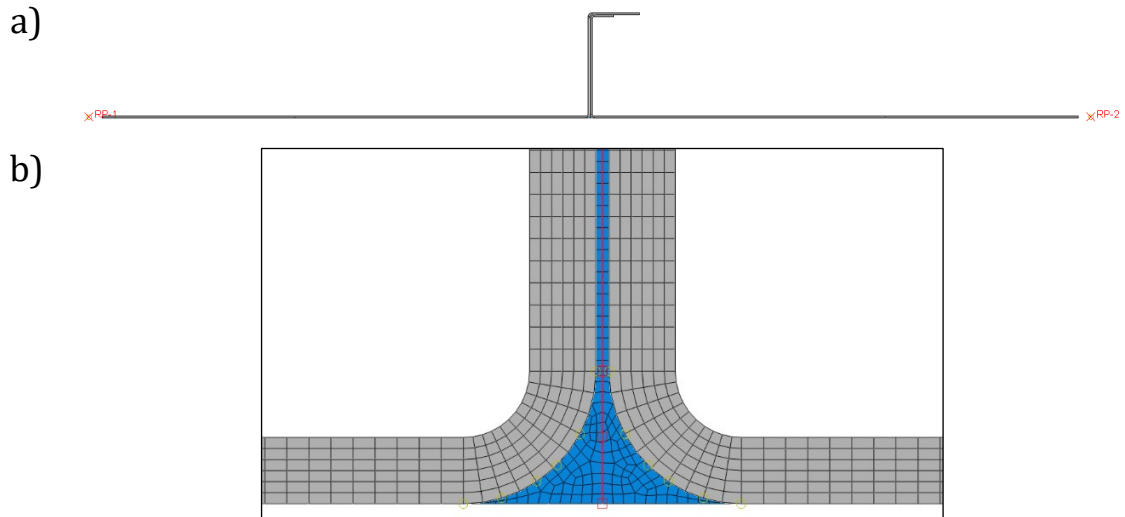
a)

b)

Figure 16: (a) Numerical model of the adhesively bonded sub-structure test; (b) Details of the adhesive FE modelling in the sub-structure.
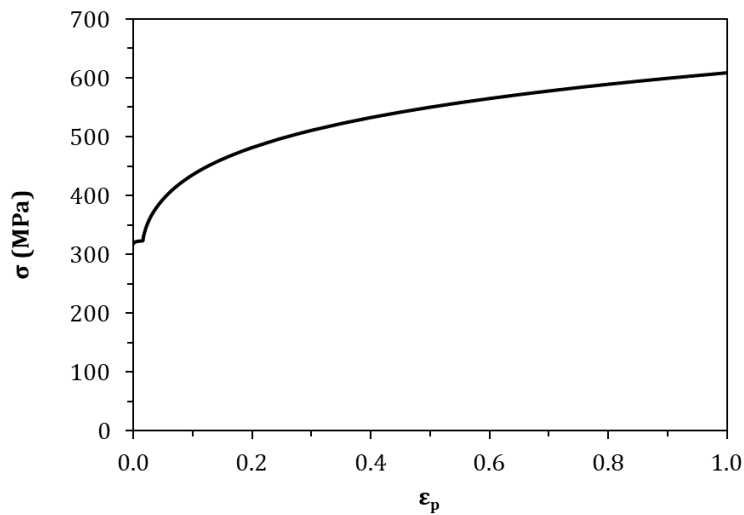

Figure 17: Flow curve (true stress vs. plastic strain) of DD11 steel.

Being the stiffness of the gripping system excluded from the experimental-numerical comparison, this part was modelled as a line of nodes rigidly connected to reference

points (RP-1 and RP-2 in Figure 16a), constrained along all the degrees of freedom, except in the horizontal direction, where the displacement was imposed to RP-2. The resulting load P and displacement δ was evaluated at this reference point.

As shown in the detail of the model in Figure 16b, the adhesive completely filled the gap left by the curvature of the panels. Considering the peculiar geometry of this adhesive layer, a continuum cohesive approach with only one element through the thickness would have generated excessively stretched elements. For this reason, a local cohesive approach was chosen instead. In this case, adhesive degradation and failure was modelled by a contact interaction, with a cohesive behaviour (highlighted in red in Figure 16b), between two continuum CPE4R elements layers (in blue in Figure 16b). Therefore, a free mesh control technique could be used for the adhesive close to panels curvature. Tie constraints were used to connect the adhesive layers to the panels and master and slave roles were assigned to adherends and adhesive layers, respectively.

For the contact with cohesive behaviour, the cohesive parameters of Table 5 were used, except for the stiffness parameters e_i. In fact, as previously discussed, in this case, e_i lose their physical meaning and they must be chosen as large as possible (a value of 10^6 MPa/mm was set). Conversely, the deformation of the adhesive was simulated by the continuum elements of the adjacent layers. For these elements a Poisson's modulus v of 0.35, typical of epoxy adhesive, was chosen. Young's modulus E was derived from the previously obtained parameters e_I, using Eq. (3). Given the geometrical thickness t_A of 0.3 mm of the cohesive elements used for obtaining e_I (2114 MPa), the resulting E is equal to 634.2 MPa. This value was assigned to the continuum elements of the adhesive.

Finally, a cohesive viscosity parameter μ was used to help the convergence rate of simulations during the softening regime. This is commonly done, as reported in [17], as

36

long as it is proven that the chosen value does not influence the results in terms of the load vs. displacement curve.

Computations that use cohesive zones to model crack nucleation often experience convergence issues at the point where the crack first nucleates. These problems are known to arise from an elastic snap-back instability, which occurs just after the stress reaches the peak strength of the interface. In an implicit finite element formulation, it can be derived that the radius of convergence reduces to zero at the point of instability. In an explicit scheme, the solution quickly diverges from the equilibrium path and leads to unphysical predictions. Gao and Bower [46] proposed a simple method to completely avoid convergence difficulties by introducing a small fictitious viscosity in the cohesive zone law that characterizes the interface, permitting stresses to be outside the limits set by the TSL. Therefore, a viscous stiffness degradation D_v can be used instead of D, defined in Eq. (5). The two matrices are related through Eq. (24), where $\dot{D}_v$ is rate of change in the damage variable, the aforementioned μ represents the relaxation time of the viscous system and D stands for the degradation variable evaluated in the inviscid backbone model.

$$\dot{D}_v = \frac{1}{\mu}(D - D_v) \tag{24}$$

The use of viscous regularization of the constitutive equations makes the tangent stiffness matrix of the softening material to be positive definite for sufficiently small-time increments. More details on convergence problems and viscous regularization can be found in [46].

This method is implemented in Abaqus™, in which the response of the damaged material can be evaluated using the viscous degradation variable [15]. Using viscous regularization with a small value (compared to the time increment) of the viscosity parameter μ can improve the rate of convergence in the presence of a softening regime

37

without compromising the accuracy of the results. A value of $\mu = 10^{-5}$ Ns/mm was set, as Khoramishad *et al.* [47] proved that this value of viscosity allows surpassing the divergent behaviour of the solution without changing the overall results.

4.3. Results

Results of the comparison between experiment and numerical simulation of the full-scale sub-structure are shown in Figure 18. An excellent agreement of the initial slope was achieved, whereas the maximum reached load was underestimated approximately by 11%, in favour of safety. The numerical simulation was run using the quadratic nominal stress and the linear power law criteria, but no distinguishable difference was obtained varying both damage initiation and fracture criteria, because the full-scale sub-structure is loaded in mode I in this test configuration.
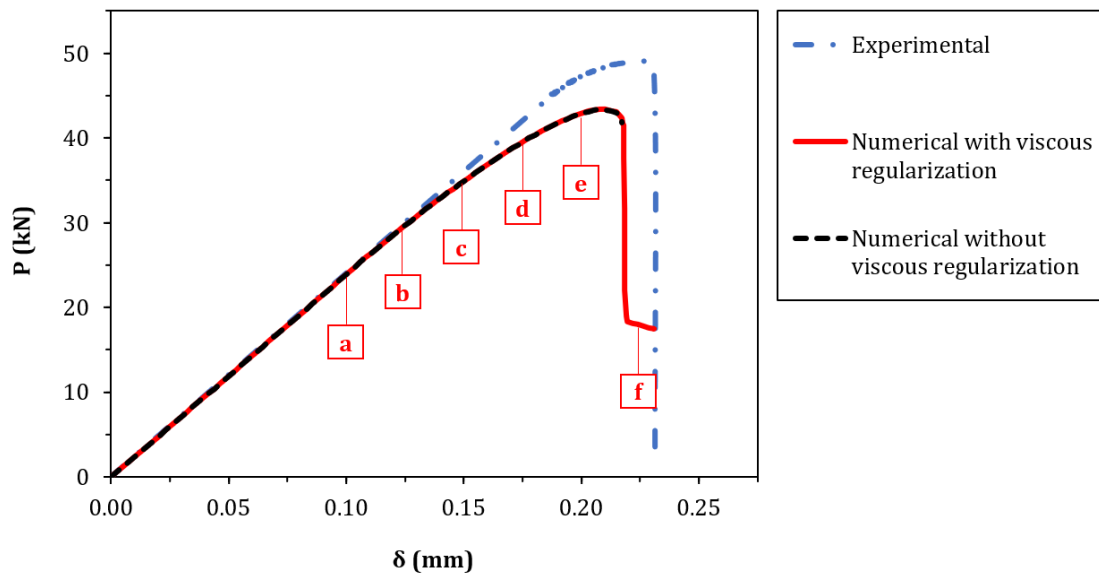

Figure 18: Experimental-numerical comparison of the load vs. displacement curves of the full-scale sub-structure testing. Letters refer to the different situations reported in Figure 19.

It is worth to mention that the chosen value of μ in the numerical analysis with the viscous regularization was proven to help the numerical convergence in the adhesive

softening phase, without affecting the values of the P-δ curves. In fact, without viscosity (setting $\mu = 0$ Ns/mm), the same shape of the curve was obtained, except that the simulation aborted right after the adhesive failure, as shown by the black dashed line.

Figure 19 shows in detail the sequence of the opening of the full-scale sub-structure obtained by simulation. The points on the load vs. displacement curve are indicated in Figure 18 by the corresponding letters. Between point b and c, the adhesive started to fail, as some internal nodes of the two layers of adhesive were released by the cohesive contact. From c to e, a void grew in the adhesive layer. The outermost part of the adhesive (the lower part in Figure 19) barely contributed to the load transmission between the two metallic parts. A limited yielding was experienced by the panels in the simulation, but the increase of compliance in the load vs. displacement curve (approximately from points b to e in Figure 18) was due to the reduction of the connected area in the bondline. The occurrence of internal void in the adhesive layer was impossible to be detected during the experimental test, but this may have occurred at a higher load, as deduced from the experimental curve in Figure 18. This increase of compliance at dissimilar loads might be due to a difference between the FE model and the actual geometry of the adhesive in the full-scale sub-structure, considering the possible defects and misalignments of a handmade bonding.

The size of the PZ could not be evaluated accurately with the proposed modelling technique based on cohesive contact interaction, as we found that only one pair of nodes enters the damage regime of the TSL, for any crack length and any mesh size in the 0.125 – 0.3 mm range. To evaluate the PZ size, the cohesive contact interaction had to be replaced by a thin layer of cohesive elements. By this approach, a P-δ curve very close to that shown in Figure 18 was obtained and the size of the PZ between points b and c could be evaluated as about 4.00 mm wide.

39

a) $\delta \approx 0.100$ mm

b) $\delta \approx 0.125$ mm

c) $\delta \approx 0.150$ mm

d) $\delta \approx 0.175$ mm

e) $\delta \approx 0.200$ mm
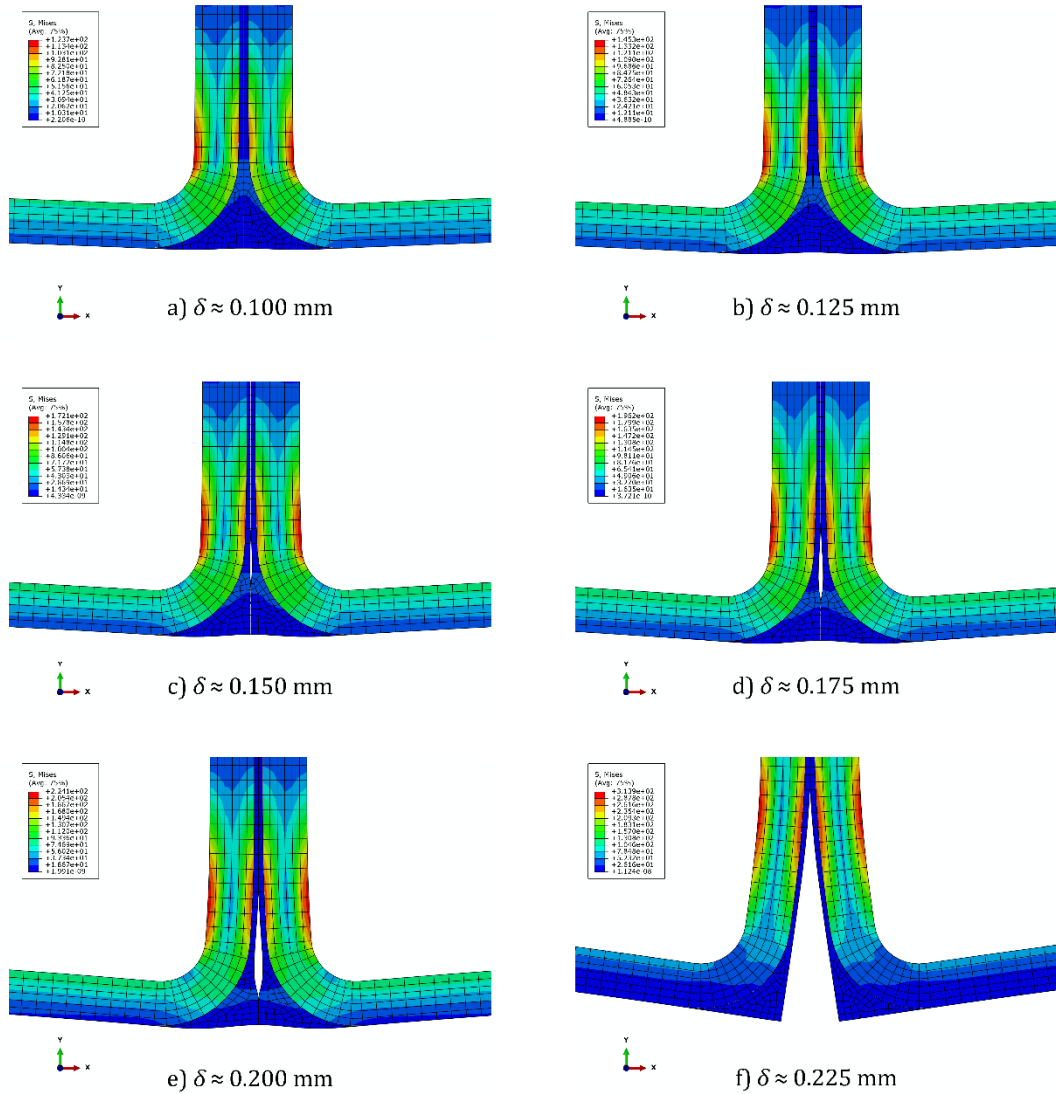
f) $\delta \approx 0.225$ mm

Figure 19: Numerical simulation of the full-scale sub-structure opening at different imposed displacements. The positions in the load vs. displacement curve of Figure 18 are indicated by the corresponding letters. Deformations are magnified by the scale factor of 10.

Another possible explanation for the different maximum load reached during the experiment and the value predicted by FE simulation might be the different curing cycle of the sub-structure. The latter was cured for 28 days at about 25°C, while DCB and ENF specimens were cured for 3 hours at 60-65°C. Therefore, the cohesive parameters of the

40

epoxy obtained through DCB and ENF tests could not be completely representative of the behaviour of the adhesive cured at room temperature.

It is also worth to mention that the 2D model does not perfectly replicate the real 3D object. Finally, in the simulation, further debonding of the sub-structure occurred after the first drop of the load (point *f* in Figure 18 and Figure 19). However, it was not possible to see this in the real sub-structure, because the test was stopped as soon as the testing machine sensed the first load drop (ending point of the experimental curve in Figure 18). The test was not extended beyond this point because this condition was unacceptable for the application for which the joint was designed.

5. Conclusions

The experimental and numerical study performed on the 3M Scotch-Weld™ 7260 B/A epoxy resin allowed to obtain the parameters of a cohesive damage model to predict and simulate degradation and failure of the adhesive by finite element analyses. DCB and ENF tests allowed to calculate the critical strain energy release rates G_{Ic} and G_{IIc}. Assuming a triangular shape of the TSL, suitable for brittle adhesives, the other cohesive parameters e_i and $\sigma_{u,i}$ were evaluated through a numerical optimization technique, by an inverse method, i.e. by iterative curve fitting of test data.

G_{Ic} and G_{IIc} resulted to be 1.07 N/mm and 6.63 N/mm, with a ratio G_{IIc}/G_{Ic} equal to 6.2. Values between 6 and 10 are reported in the literature [48,49] for high toughness epoxies.

The numerical simulations of the test on a full-scale adhesively bonded sub-structure with cohesive elements and parameters obtained from DCB and ENF tests, confirmed the validity of the cohesive damage model approach. Results agreed with experiments, as

41

long as mesh size was lower or comparable with PZ size. However, an element size at least one order of magnitude lower than PZ size is strongly recommended.

The performance of the cohesive damage model is encouraging for a future design of adhesive joints using only numerical models in place of long and expensive experimental tests. However, the validation of the mixed-mode initiation damage and fracture criteria should be further investigated, since the application regarded a full-scale sub-structure loaded in mode I. This investigation might be conducted on other full-scale sub-structures, in which the load composition includes both mode I and mode II. Another limitation highlighted by the experimental-numerical comparison consists of the dissimilar geometries between the FE models and the geometries of handmade adhesive layers of real parts. This could introduce a not-negligible error in the maximum reached load of the sub-structure, thus a FE modelling in favour of safety is always recommended.

It must be emphasised that the characterization of the epoxy resin presented in this paper is limited to room temperature. This work does not consider all the environmental conditions, such as temperature and relative humidity, and do not account for loading rate and curing temperature effects, which are well known to influence the behaviour of polymeric adhesives. The knowledge of the dependence of the cohesive parameters upon these effects is crucial for realistic engineering applications. An ongoing work is focusing on the influence of temperature on the cohesive parameters of the studied epoxy.

Further experimental tests on bulk adhesive specimens need being conducted to directly measure the cohesive parameters e_i to confirm the validity of the values obtained with the numerical optimisation. Additionally, regarding the optimization of the cohesive parameters by means of the software Isight™, minimization of the error of the crack length a vs. displacement δ data might also be considered, instead of the P-δ data used in

42

this work. Finally, experimental tests based on direct methods could be performed for the evaluation of the cohesive parameters to be compared to the ones identified in this work.

References

[1]   Habenicht G. Applied Adhesive Bonding: A Practical Guide for Flawless Results. Weinheim: WILEY-VCH Verlag GmbH & Co KGaA; 2009.

[2]   Adams RD, Wake WC. Adhesive Joints in Engineering. 2nd ed. London: Elsevier Applied Science; 1986.

[3]   da Silva LFM, Ochsner A. Modeling of Adhesively Bonded Joints. Berlin: Springer; 2008.

[4]   Elices M, Guinea GV, Gómez J, et al. *Eng. Fract. Mech.* 2002;69:137–163.

[5]   Moura MFSFD, Gonçalves JPM, Marques AT, et al. *Compos. Struct.* 2000;50:151–157.

[6]   Petrossian Z, Wisnom MR. *Compos. Part A Appl. Sci. Manuf.* 1998;29:503–515.

[7]   Mi Y, Crisfield MA, Davies GAO, et al. *J. Compos. Mater.* 1998;32:1246–1272.

[8]   Schwalbe KH, Scheider I, Cornec A. Guidelines for Applying Cohesive Models to the Damage Behaviour of Engineering Materials and Structures. New York: Springer; 2013.

[9]   Siegmund T, Brocks W. *Int. J. Fract.* 1999;99:97–116.

[10]   Scheider I, Brocks W. *Eng. Fract. Mech.* 2003;70:1943–1961.

[11]   Brocks W, Scheider I, Schödel M. *Arch. Appl. Mech*. 2006;76:655–665.

[12]   Scheider I, Brocks W. *Eng. Fract. Mech.* 2008;75:4001–4017.

[13]   Scheider I, Brocks W. *Comput. Mater. Sci.* 2006;37:101–109.

[14]   Brocks W. Computational Fracture Mechanics. In: Raabe D, Roters F, Barlat F, et al., editors. Contin. Scale Simul. Eng. Mater. Weinheim: WILEY-VCH Verlag

GmbH & Co KGaA; 2004. p. 606–622.

[15] Dassault Systèmes. Abaqus^{TM} User's Documentation 6.12. Vélizy-Villacoublay; 2012.

[16] de Moura MFSF, Campilho RDSG, Gonçalves JPM. *Int. J. Solids Struct.* 2009;46:1589–1595.

[17] da Silva LFM, Campilho RDSG. Advances in Numerical Modeling of Adhesive Joints. Heidelberg: Springer; 2012.

[18] Campilho RDSG, Banea MD, Pinto AMG, et al. *Int. J. Adhes. Adhes.* 2011;31:363–372.

[19] Campilho RRDSG, de Moura MMFSF, Domingues JJMS. *Compos. Sci. Technol.* 2005;65:1948–1958.

[20] Campilho RDSG, de Moura MFSF, Domingues JJMS. *Int. J. Solids Struct.* 2008;45:1497–1512.

[21] Gonçalves JPM, de Moura MFSF, de Castro PMST, et al. *Eng. Comput.* 2000;17:28–47.

[22] de Moura MFSF, Gonçalves JPM, Marques AT, et al. *J. Compos. Mater.* 1997;31:1462–1479.

[23] American Society for Testing and Materials International. ASTM D3433-99, Standard Test Method for Fracture Strength in Cleavage of Adhesives in Bonded Metal Joints. West Conshohocken; 2012.

[24] International Organization for Standardization (ISO). ISO 25217, Adhesives — Determination of the mode 1 adhesive fracture energy of structural adhesive joints using double cantilever beam and tapered double cantilever beam specimens. Geneva; 2009.

[25] da Silva LFM, Dillard DA, Blackman B, et al. Testing Adhesive Joints Best

Practices. Test. Adhes. Joints Best Pract. Weinheim: WILEY-VCH Verlag GmbH & Co KGaA; 2012.

[26]   Rice JR. *J. Appl. Mech.* 1968;35:379.

[27]   Cherepanov GP. *Appl. Math. Mech.* 1967;31:476–488.

[28]   Olsson P, Stigh U. *Int. J. Fract.* 1989;41:71–76.

[29]   Andersson T, Stigh U. *Int. J. Solids Struct.* 2004;41:413–434.

[30]   da Silva LFM, Adams RD, Gibbs M. *Int. J. Adhes. Adhes.* 2004;24:69–83.

[31]   Högberg JL, Stigh U. *Eng. Fract. Mech.* 2006;73:2541–2556.

[32]   Leffler K, Alfredsson KS, Stigh U. *Int. J. Solids Struct.* 2007;44:530–545.

[33]   Högberg JL, Sørensen BF, Stigh U. *Int. J. Solids Struct.* 2007;44:8335–8354.

[34]   Chai H. *Exp. Mech.* 1992;32:296–303.

[35]   Flinn BD, Lo CS, Zok FW, et al. *J. Am. Ceram. Soc.* 1993;76:369–375.

[36]   Mello AW, Liechti KM. *J. Appl. Mech. Asme.* 2006;73:860–870.

[37]   Li S, Thouless MD, Waas AM, et al. *Compos. Sci. Technol.* 2005;65:537–549.

[38]   Campilho RDSG, de Moura MFSF, Domingues JJMS. *Int. J. Adhes. Adhes.* 2009;29:195–205.

[39]   Carlberger T, Stigh U. *J. Adhes.* 2010;86:814–833.

[40]   3M Industrial Tapes & Adhesives Department Laboratory. Scotch-Weld[TM] 7260 B/A Series: Technical Data Sheet. 2003.

[41]   3M France Techniques Adhésives Industrielles. Scotch-Weld[TM] 7260 B/A: Bulletin Technique [Technical Bulletin] BT 0905-0203 (in French). 2003.

[42]   Krenk S. *Eng. Fract. Mech.* 1992;43:549–559.

[43]   de Moura MFSF, Silva MAL, de Morais AB, et al. *Eng. Fract. Mech.* 2006;73:978–993.

[44]   Torczon V, Lewis RM, Trosset MW. *J. Comput. Appl. Math.* 2000;124:191–207.

45

[45]   European Standard. EN 10111:2008 - Continuously hot rolled low carbon steel sheet and strip for cold forming - Technical delivery conditions. Brussels; 2008.

[46]   Gao YF, Bower AF. *Model. Simul. Mater. Sci. Eng.* 2004;12:453–463.

[47]   Khoramishad H, Crocombe AD, Katnam KB, et al. *Int. J. Fatigue.* 2010;32:1146–1158.

[48]   Saldanha DFS, Canto C, Da Silva LFM, et al. *Int. J. Adhes. Adhes.* 2013;47:91–98.

[49]   Banea MD, da Silva LFM, Campilho RDSG. *J. Adhes.* 2012;88:534–551.